Trends in Analytical Chemistry 180 (2024) 117904

Contents lists available at ScienceDirect

Trends in Analytical Chemistry

journal homepage: www.elsevier.com/locate/trac

Transient OCP-apatite epitaxy controls bone mineralization. An X-ray total scattering study

Federica Bertolotti [a], Jan Skov Pedersen [b], Alexander Van Driessche [c], Norberto Masciocchi [a], Antonietta Guagliardi [d,*], José M. Delgado-López [e,**]

[a] Dipartimento di Scienza e Alta Tecnologia and To.Sca.Lab, Università dell'Insubria, Como, Italy
[b] Interdisciplinary Nanoscience Center (iNANO) and Department of Chemistry, Aarhus University, Aarhus C, Denmark
[c] Instituto Andaluz de Ciencias de la Tierra (IACT, CSIC-UGR), Armilla, Granada, Spain
[d] Istituto di Cristallografia and To.Sca.Lab, CNR, Como, Italy
[e] Department of Inorganic Chemistry, Faculty of Science, University of Granada, Granada, Spain

ARTICLE INFO

Keywords:
Collagen mineralization
Bone
Epitaxy
Wide-angle X-Ray total scattering
Debye scattering equation
Small-angle X-ray scattering

ABSTRACT

Despite the biological relevance and the unique mechanical properties of bone tissue, the pathway leading to the formation of the main mineral component – specifically, the mechanism responsible for the formation of extremely thin apatite nanoplatelets – remains unclear. In this work, the presence and evolution of an elusive octacalcium phosphate/apatite (OCP/Ap) heterostructure is identified through the combination of small- and wide-angle X-ray total scattering experiments. These experiments were performed *in situ* during collagen mineralization, and the structure, morphology, and epitaxy of these nanocrystalline composites are described using atomistic models. By applying the Debye Scattering Equation to our high-quality synchrotron X-ray scattering datasets, a quantitative estimate of the size and shape of the nanoplates, as well as their temporal evolution, is achieved. The transformation of this transient heterostructure is revealed through confocal Raman microscopy to occur within the intrafibrillar spaces of the collagen fibers. As mineralization progresses, these spaces gradually cluster, resulting in a *ca.* 60 % increase in the lateral density of the purely organic molecular bundles. In contrast, in dry collagen, the mineralization process induces a (marginal) decrease in bundles density. Despite their apparent opposite, we present an explanation that reconciles both effects.

1. Introduction

Bone is a multilevel hierarchical hard tissue [1–5]. The basic building blocks of this complex architecture are mineralized collagen fibrils, a periodic array of self-assembled triple collagen helices [4] that are reinforced with uniaxially aligned apatite nano-platelets [1,4,6]. During collagen mineralization *in vivo*, mineral deposition occurs both inside (intrafibrillar) and outside (inter- or extra-fibrillar) collagen fibrils through apparently different mechanisms. Over the past years, significant progress was made towards the understanding of the molecular mechanisms underlying bone mineralization. However, an ongoing debate persists concerning the chemical nature of the first mineral phase formed, the factors that govern the initial deposition and growth of crystals, and the specific role of the organic matrix (including collagen, non-collagenous proteins, NCPs, citrate and other small molecules) [7]. Numerous studies have investigated the role of collagen and NCPs, confirming their involvement in different stages of bone mineralization. These stages encompass the formation of the amorphous calcium phosphate (ACP, $Ca_3(PO_4)_2{\cdot}nH_2O$ [8]) precursor, its further transformation into nanocrystalline phases, and the subsequent organization of apatite nanocrystals [7,9,10]. It has been repeatedly proposed that the collagen matrix plays an active role, acting alone or in synergy with NCPs. It is generally accepted that intrafibrillar mineralization occurs via a non-classical nucleation mechanism involving the precipitation of amorphous precursors, which infiltrate into the nanoscopic holes of the gaps and further transform into nanocrystalline apatite (Ap), preferentially aligned with the *c*-axes parallel to the longitudinal axis of the fibrils.

The extremely thin nature, from ~15 to 35 Å [2,4,11], of the mineral phase plays a pivotal role in the biomechanical properties of bone tissue

* Corresponding author.
** Corresponding author.
E-mail addresses: antonietta.guagliardi@cnr.it (A. Guagliardi), jmdl@ugr.es (J.M. Delgado-López).

https://doi.org/10.1016/j.trac.2024.117904
Received 7 September 2023; Received in revised form 6 June 2024; Accepted 6 August 2024
Available online 14 August 2024

[12,13]. Noteworthy, to achieve this typical plate-shaped morphology of bone apatite, the intrinsic hexagonal symmetry of apatite must be broken [14–16]. It has been proposed that some of the organic molecules present in bone organic matrix (*e.g.*, citrate), are mainly responsible for the formation of these thin plates, through specific adsorption or formation of transient templates [17–19]. However, the formation of these very thin plates has also been observed in the absence of organic additives [20].

Another possible explanation is that the thin nature of the mineral is reminiscent of an unstable transient precursor formed at the early stages of mineralization. The current view of bone mineralization assumes that ACP nano-spherulites [21,22] are the first particles to form, which, upon maturation, gradually transform into thin apatite platelets. Alongside ACP, a transient octacalcium phosphate phase [OCP, $Ca_8H_2(PO_4)_6 5H_2O$], which crystallizes as thin blades of triclinic crystal symmetry (space group P1) has also been identified as a possible precursor of apatite in bones and teeth [23–25] and dental calculus. This fact also explains the well-known calcium-deficiency of biological apatites [18,26], as well as their plate-like morphology [27]. However, how and to what extent these transient phases control the final atomic arrangement, the morphology and the chemical composition of the apatite nanoplatelets remains an unsolved issue.

The mineralization of collagen *in vitro* has traditionally been of interest both for understanding the processes behind bone formation (*in vivo*) and as a source of inspiration for the synthesis of biomimetic scaffolds for tissue engineering [7]. *In vitro* collagen mineralization experiments in the presence of molecules present in bone (*e.g.*, collagen, non-collagen proteins, citrate, carbonate, etc.) have traditionally been used as useful models to gain new insights into the molecular mechanisms of bone mineralization. However, it must be considered that this is a simplified experimental approach to the very complex process occurring *in vivo,* where several biochemical processes take place simultaneously.

Studying *in situ* mineral growth processes from solution or in suspension with the aim of gathering robust size-, shape- and crystal phase properties can be achieved through advanced scattering methods, such as small-angle X-ray scattering (SAXS) or wide-angle X-ray total scattering (WAXTS) techniques. The combined use of these methods makes it possible to determine morphological and structural details across a wide range of scales, ranging from the nanometer to the sub-picometer scale under favorable conditions. Applications of this approach can be found for inorganic nanoparticles (cementitious binders [28], colloidal quantum dots [29,30], perovskites [31,32]), and, notably, in the detailed structural characterization of biomimetic materials based on calcium phosphate [33–35].

In this work, we monitored *in situ* the mineralization of dense collagen matrices at different length-scales, combining synchrotron-based WAXTS (analysed by the Debye Scattering Equation formalism - DSE), SAXS, confocal Raman spectroscopy, and scanning electron microscopy (SEM) imaging. We observed the formation of epitaxially-grown heterostructures of OCP and Ap thin nanoplates, which gradually reorganize into Ap while retaining their initial platy morphology. Simultaneously, a gradual contraction of the lateral packing of the collagen macromolecules inside the fibrils occurs, which is triggered by mineral growth in the intrafibrillar space. In the following, the results from various complementary techniques are discussed, towards a unifying model of Ap nanocrystal growth that accounts for all our experimental observations. Moreover, the validity of literature models of the OCP/Ap epitaxy is critically evaluated and the crystal-phase and morphological evolution in the early stages of mineralization are carefully analysed.

2. Results and discussion

2.1. In situ monitoring of collagen mineralization

Mineralization experiments were carried out in dense collagen matrices at physiological conditions (pH 7.4 and 37 °C, further details of the mineralization protocol are provided in the Methods section). The calcium concentration ($[Ca^{2+}] = 2.5$ mM) was selected to obtain a low degree of mineralization enabling to monitor the evolution of both collagen and mineral components across different length scales by *in situ* SAXS and WAXTS (Fig. S1). The obtained data allowed us to reconstruct the structural evolution of the mineral phase upon maturation inside a collagen matrix. Fig. 1a shows the WAXTS patterns collected soon after (<15 min) injecting the just mixed calcium- and phosphate-containing solutions into collagen (t_0 in Fig. 1a–c) and at selected times up to 40 h of collagen mineralization. The mineral phase apparently exhibits the crystalline structure of apatite; however, some subtle, but measurable features at a scattering vector modulus of $Q = 0.67$ Å^{-1} (Fig. 1b) and $Q = 1.83$ Å^{-1} (Fig. 1c) also suggest the presence of non-apatitic (but OCP-like) domains during the initial stages of mineralization (t_0 and 1h). The broad peak at $Q = 0.67$ Å^{-1} is indeed characteristic of the 1–10/010 OCP doublet. This peak *gradually* shifts towards higher Q-values upon maturation (Fig. 1b–d) and after 20 h it matches the position of the 100 reflection of bone Ap (Fig. 1c and d). The observation that the OCP doublet is not vanishing while the 100 Ap peak is simultaneously growing, is in line with a "structural interference" (later discussed) and a progressive material modification through intermediate stages, where OCP and Ap do not co-exist as separate phases. Concomitantly, the 002 peak of the initial nanocrystalline mineral phase moves towards lower Q values, suggesting the progressive expansion of the structural periodicity of the (initially formed) mineral along the *c*-axis (Fig. 1d).

We also found that organic additives other than collagen, such as citrate and polyaspartate, pAsp, slow down the kinetics of the reaction but do not alter the mineralization pathway. Indeed, the same mineralization experiments with WAXTS were carried out by adding carbonate, carbonate/citrate and carbonate/pAsp (Fig. S2) or in the absence of collagen (Fig. S3). Our *in-situ* observations revealed that in all these cases the proposed pathway is not altered, with the persistent formation of the transient OCP/Ap heterostructure, ending up in the formation of bone-like nanocrystalline apatite (Fig. S2 and Fig. S3). These results also indicated that the collagen matrix cannot be taken as the responsible for the formation of the OCP-like structure at the early stages of mineralization, since it was also identified in the absence of the protein (Fig. S3).

The precipitation of ACP at the early stages was not detected under the aforementioned experimental conditions ($[Ca^{2+}] = 2.5$ mM). However, the formation of ACP was observed at t_0 when $[Ca^{2+}]$ was increased up to 40 mM (Fig. 1e). Then, a similar mineralization pathway, involving the co-existence of the OCP-like and Ap domains was detected at $t = 1$h (Fig. 1e and f). We therefore speculate that, being the OCP/Ap heterostructure the first phase detected under low $[Ca^{2+}]$ experimental conditions, the ACP is undetected in these conditions since the short persistence of the amorphous phase in phosphate-rich solutions [36] results in a fast crystallization of ACP into the transient OCP/Ap heterostructure. In conclusion, this transient OCP/Ap heterostructure is systematically observed and upon maturation undergoes a rapid conversion into nanocrystalline apatite regardless of the Ca concentration or the presence of additional organic additives.

The morphological evolution of calcium phosphate nanoparticles was also monitored by *in situ* time-resolved SAXS (Fig. 2). The SAXS pattern of non-mineralized collagen exhibits a Q^{-4} dependence in most of the Q-range (0.02–0.35 Å^{-1}), in line with what is predicted for the surface scattering of a typical compact object (here, the cylindrical fibrils). However, a different dependence is observed when collagen is in contact with a mineralizing solution due to the growth of mineral particles (Fig. 2a). The modelling analysis of SAXS data (see Methods) revealed a single population of extremely thin platelets (12 Å), formed

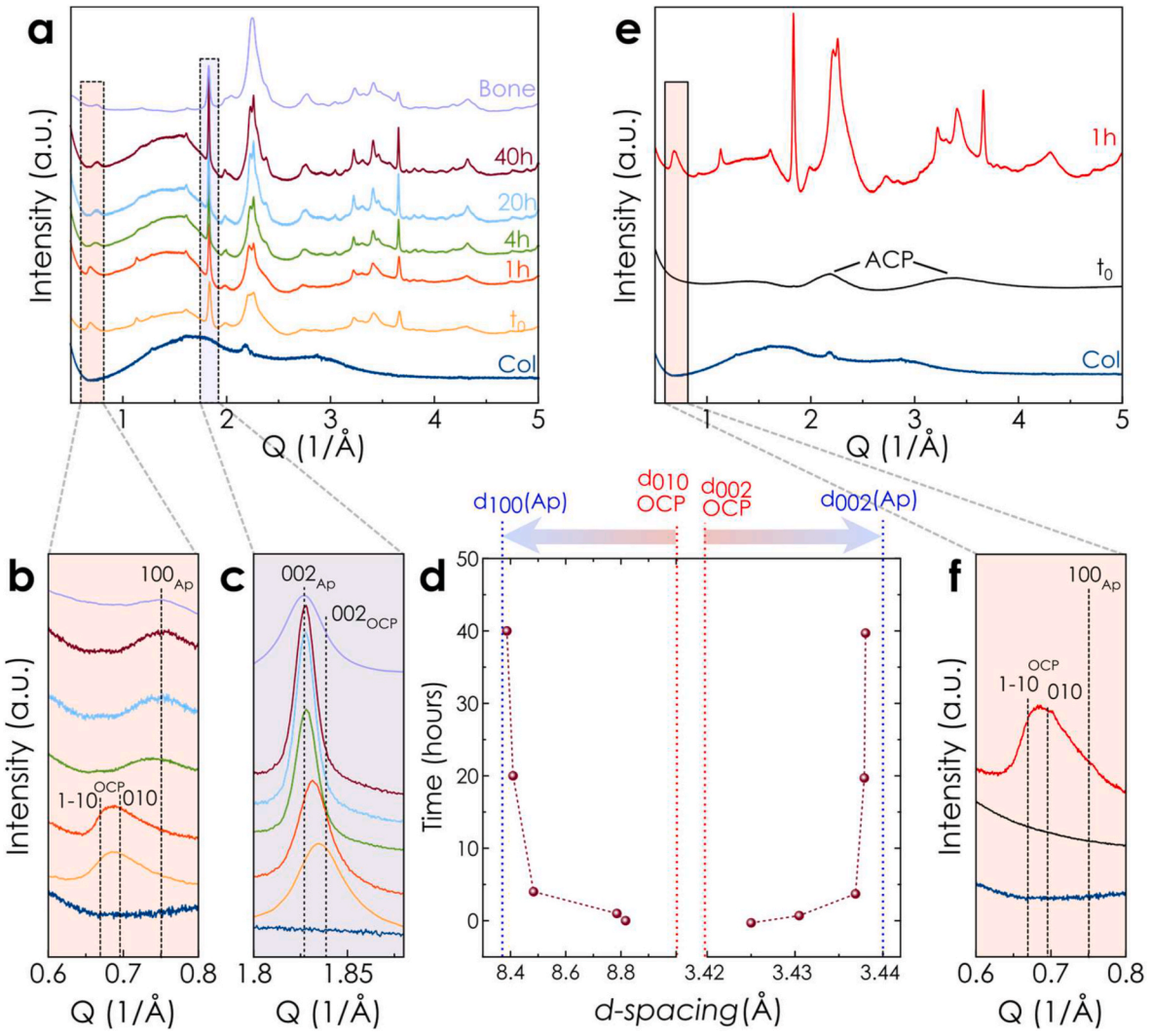

Fig. 1. Monitoring the mineralization in dense collagen matrices by WAXTS. (a) Time-dependent *in situ* WAXTS patterns of non-mineralized collagen (Col) and mineralized collagen at increasing maturation times. The pattern collected from a finely ground rabbit limb bone is shown at the top for comparison. In the bottom panels, the angular regions containing the 100 (b) and 002 (c) reflections of apatite have been magnified. (d) The broad peaks at ca. $Q = 0.67$ Å^{-1} (characteristic of the 1–10/010 OCP doublet) and 1.83 Å^{-1} (characteristic of the 002 reflection) progressively shift upon maturation confirming the presence at the early stages of the OCP/Ap assembly, which gradually transform into Ap. (e) Time-dependent *in situ* WATXS patterns of non-mineralized collagen (Col) and mineralized collagen at $[Ca^{2+}] = 40$ mM at t_0 and 1 h and the corresponding angular region containing the 100_{Ap} reflection (f).

during the early stages of mineralization, which, within a few hours, thicken to 20 Å and then gradually reach the final ~25 Å thickness (Fig. 2b). Similar results, but up to a 15 Å nanoplate thickness after 14 h of maturation time, are reported for the mineralization process deliberately retarded by adding polyaspartic acid in a simulated body fluid solution [37]. Our parallel WAXTS experiments reveal the progressive vanishing of the 010 reflection of OCP ($Q = 0.69$ Å^{-1}), concomitantly with the increase of the intensity of the 100 reflection of Ap ($Q = 0.75$ Å^{-1}) and the low-angle shift of the 002 peak position (Fig. 1a–c).

In the collagen mineralization experiments (see Methods) the following features are systematically observed: i) the precipitation of a polydisperse population of nanoplates with a polydisperse thickness, with average thickness in the limited 12–27 Å range; ii) a concomitant decrease and increase of the OCP and Ap mineral character, respectively, when mineralization progresses. Significantly, OCP, present at the 37 % w/w level at the early stages (t_0), eventually disappears at longer maturation times (Table S1). Hence, the OCP-like character progressively disappears during crystal growth and the first nanocrystalline phase detected already at t_0 (discussed in section 2.2 and forming within the collagen fibrils, see section 2.3) is a heterostructure featuring epitaxy of Ap and OCP nano-domains that eventually evolves into nearly pure Ap. The formation of hybrid OCP/Ap nanoplates, instead of two independent nanocrystalline phases (*i.e.*, OCP and Ap), is confirmed with the detailed WAXTS/DSE analysis described in the next section.

2.2. WAXTS/DSE analysis of hybrid OCP/Ap nanoplatelets

To further support the hypothesis of an OCP/Ap heterostructure forming in the early stages of collagen mineralization, we have modeled both structural and morphological features using the Debye Scattering Equation, by matching our calculated WAXTS traces to the entire experimentally observed patterns. Due to the structural similarity between the OCP and Ap crystal phases, the nature and orientation of the epitaxially-shared interfaces [24,38], which are slowly reduced during mineralization because of the progressive OCP hydrolysis, must reflect well definite geometric rules. Similarly, the occurrence of the so-called "hydrated layer" on the surface of biological apatite is likely due to the incomplete conversion of OCP into Ap [18,39].

The most representative models of OCP/Ap epitaxy previously

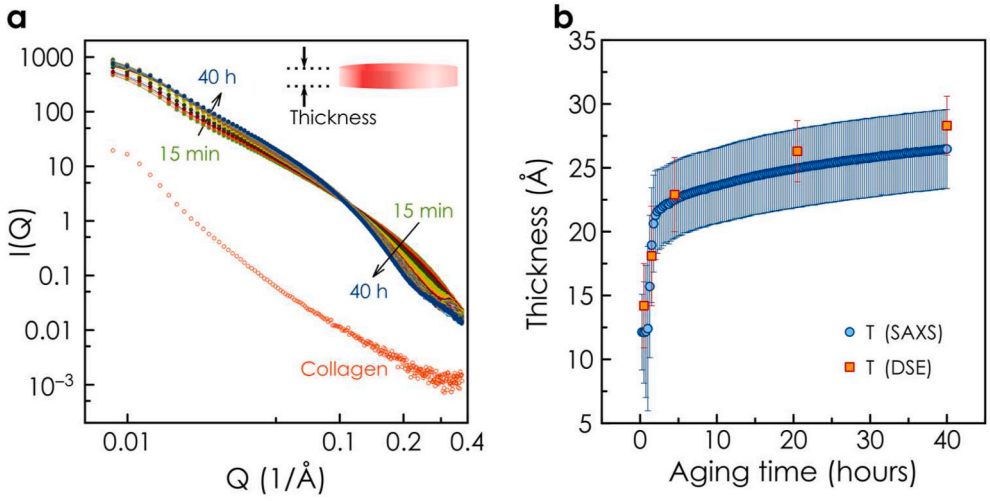

Fig. 2. Monitoring the mineralization in dense collagen matrices by SAXS. (a) Time-dependent *in situ* SAXS patterns (on a log-log scale) of pure collagen (red curve) and of the mineralized collagen at increasing maturation times. The inset sketches the model of the elliptical disks with finite thickness (*T*), used for the SAXS analysis. The corresponding fits *vs* the experimental data (coloured markers) are shown as solid lines. Note that after 1 h of mineralization the appearance of a weak Bragg peak at $Q = 0.33$ Å^{-1} points to the formation of OCP (this *Q* value corresponds to the 100 OCP reflection). The position of this peak never changes, but its intensity initially increases and after *ca.* 4 h, starts vanishing. Eventually, after 8 h of maturation, it completely disappeared. (b) Comparison of the time evolution of the thickness of the nanocrystals derived from WAXTS/DSE (orange squares) and SAXS (blue circles) data analysis. The y-error bars are the standard deviations of the lognormal (WAXTS) or Schulz (SAXS) functions used to model the nanoplatelets thickness dispersion. (For interpretation of the references to color in this figure legend, the reader is referred to the Web version of this article.)

proposed in the literature are illustrated in Fig. 3a–b. Therein, and in the following discussion, we take as reference the unit cell parameters of OCP determined by Mathew et al. [40] (triclinic *P1*, $a = 19.69$ Å, $b = 9.52$ Å, $c = 6.835$ Å, $\alpha = 90.15°$, $\beta = 92.54°$, $\gamma = 108.65°$) and, for Ap, the standard hexagonal $P6_3/m$ cell ($a = b = 9.432$ Å, $c = 6.881$ Å) [41], or small deviations therefrom, most relevant for OCP, which is a metastable phase prone to spontaneous dehydration. Brown et al. [24], originally suggested a model of OCP/Ap epitaxy in line with the $\mathbf{a}_{OCP} \sim 2\mathbf{a}_{Ap}$, $\mathbf{b}_{OCP} \sim \mathbf{b}_{Ap}$ and $\mathbf{c}_{OCP} \sim \mathbf{c}_{Ap}$ axes relationships (Fig. 3a). Later, Xin et al. [38], from *in situ* TEM examinations during OCP-to-Ap transformation, suggested an alternative model in which $\mathbf{a}_{OCP} \sim 2\mathbf{a}_{Ap}$, $\mathbf{b}_{OCP} \sim -(\mathbf{a}_{Ap} + \mathbf{b}_{Ap})$ and $\mathbf{c}_{OCP} \sim -\mathbf{c}_{Ap}$ (Fig. 3b). In both cases, a doubled $\mathbf{a}_{Ap}$ axis is indeed necessary for matching the shape and volume of the OCP unit cell. A recent revision of the OCP/Ap epitaxy model, proposed by Fernández et al. [42], is not straightforwardly comparable with the Brown et al. and Xin et al. models, but, after careful reworking, can be traced back to the axis orientations reported in Table S2. As it was found to be somewhat similar to Xin et al. model (in that $(100)_{OCP}$ is *not* aligned with $(100)_{Ap}$), this model is not further considered in our simulations.

As anticipated, our experimental WAXTS data showed the progressively vanishing and shifting of the 1–10/010 OCP doublet towards the 100 peak of Ap, the latter containing 100, 010, −110 and their centrosymmetric reflections (see Fig. 1b). This occurs simultaneously with a progressive expansion of the Ap unit cell along the *c*-axis (Fig. 1c), confirming that the OCP-to-Ap conversion progresses by epitaxial growth of Ap layers onto the OCP (010) face, until the full conversion is accomplished (4 h). This interpretation agrees with the model proposed by Xin et al. (Fig. 3b), in which OCP and Ap share their (010) faces, with the associated water (and cations) losses therefrom. At variance, for an OCP layer progressively transforming into Ap following Brown et al. model (that is, roughly along $\mathbf{a}_{OCP}$, see the graphical sketches associated with Tables S2 and S3), the progressive and continuous shift of the 010 OCP peak towards the 010 Ap signal (shown in Fig. 1b) is not expected. These observations alone thus favor the Xin et al. model, which is further supported by a subsequent structural/morphological analysis, based on pivotal experimental observations, discussed at continuation.

Indeed, taking into account the occurrence of very thin nanoplates (<15 Å thick, according to SAXS data modelling reported in Fig. 2), four different morphological/structural models can be devised, illustrated in the sketches shown in Fig. 3c and d (corresponding to the Brown model) and 3e,f (Xin model). In these drawings, a cyano-coloured plane shows the interface, while OCP and Ap are dark- and light-coloured slabs, respectively. In all four cases, the nanocrystal thickness is indicated by *T*, and the related (idealized) crystal axes orientation of the OCP phase are shown at the bottom.

Of the four possibilities drawn in Fig. 3c–f, model 3c can be easily dismissed, as it would imply a thickness *T* always larger than 20 Å (considering the $\mathbf{a}_{OCP}$ periodicity) and therefore incompatible with the SAXS results derived at the early stages of the *in-situ* growth. Model 3d contains a very small number of atoms located at the interface (falling within ±3 Å from the ideal interface, <3 % of the total, estimated by considering the experimentally derived *T*(hickness), *W*(idth) and *L* (engths) of nanoplates from DSE analysis, later discussed), a too limited value to provide a measurable intensity variation in the WAXTS pattern. A similar reasoning applies to model 3e, while, for 3f, this value falls in the 20–40 % range, and is anticorrelated with the maturation time, making thus 3f the only epitaxial model convincingly matching the structural and morphological requirements for DSE and SAXS analyses. Table S3 includes the *T*, *W*, *L* parameters, as well as the volume ratio of the interface region *vs.* total nanoplates volume.

Consequently, prior to DSE analysis, atomistic models of nanocrystals were built using the Xin et al. model (as per Fig. 3f and Fig. S4), with the thickness of OCP fixed at one OCP unit cell along the **b** axis, while along the other two directions (**a** and **c**) a population of nanoplates of variable-size was used, paralleling that of the blanketed Ap nanoplates to which they are attached (*vide infra*). This atomic-to-nanometer unified approach allows the simultaneous modeling of the mutual orientation of Ap and OCP structures and of the orientation of the nanodomains epitaxy with respect to the platy morphology. The thickness of the OCP/Ap nanoplates is iteratively adjusted and matched to the thicknesses obtained from the SAXS fits (see Methods) that are insensitive to the atomic scale. Details of the atomistic OCP/Ap model are provided in the SI. WAXTS/DSE analysis (Fig. 3g and h) excluded the biphasic model (*i.e.*, OCP and Ap growing as independent phases) in favor of the OCP/Ap Xin's epitaxy model. Fig. 4 shows the final DSE fits and the progressive size evolution of the OCP/Ap heterostructure, all

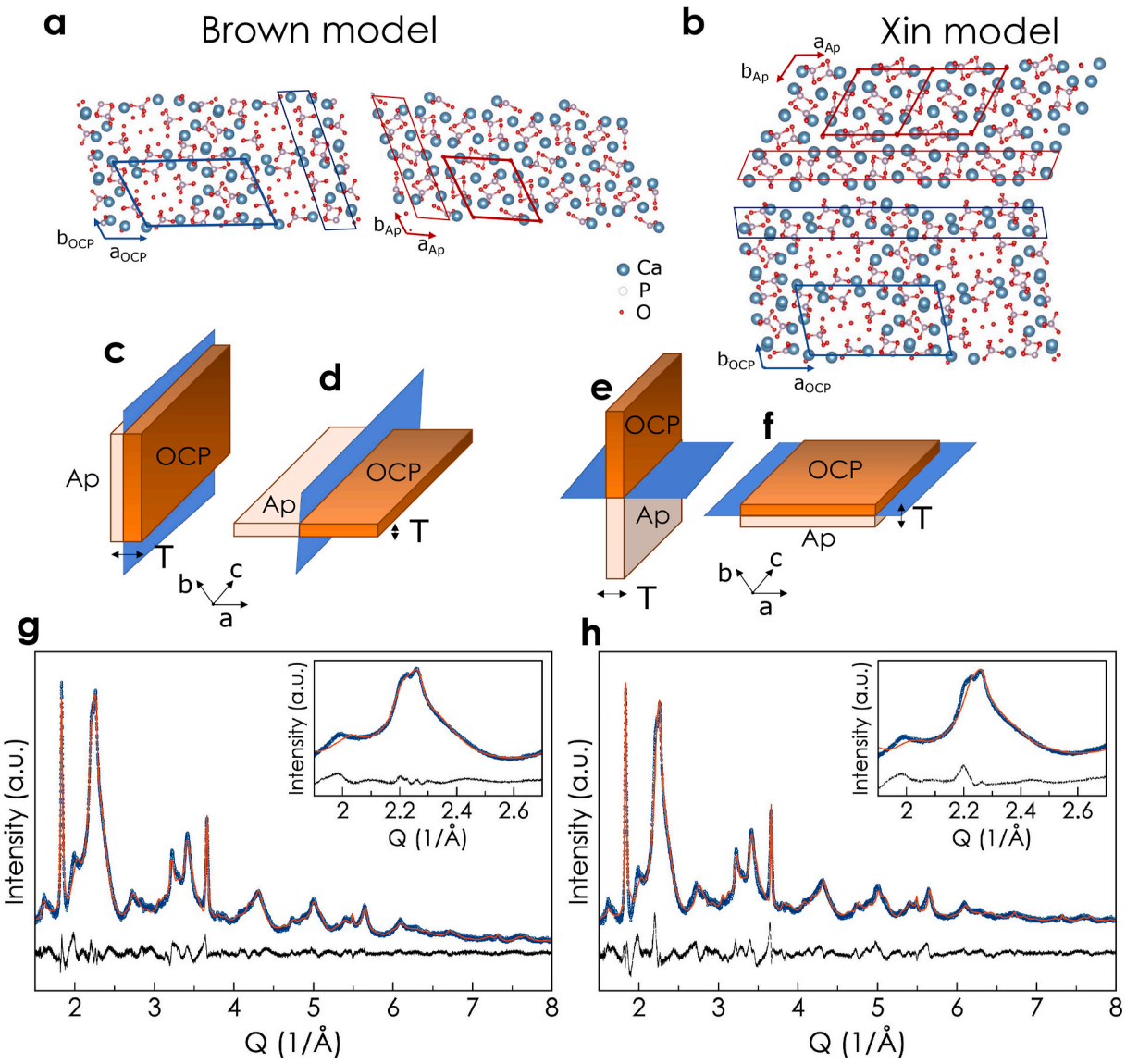

Fig. 3. Structural relations of the OCP epi-layer (blue) on top of an Ap (red) surface: a) Brown's model; b) Xin's model. The unit cell sizes and orientations are also sketched. c,d,e,f) Four different structure/morphology orientations: c,d) Brown's model; e,f) Xin's model. The cyano planes are the interfaces separating two bricks of OCP and Ap (dark- and light-coloured, respectively). Best fits for the WAXTS data (blue dots) at t_0 obtained using the DSE simulations (red lines) of the OCP/Ap epitaxy according to g) Xin's model (goodness of fit, $[GOF = (\chi^2)^{1/2}] = 1.42$) and h) a biphasic model ($GOF = 2.08$). (For interpretation of the references to color in this figure legend, the reader is referred to the Web version of this article.)

nanoplates possessing a single (9 Å thick) monolayer of OCP epitaxially grown by sharing the large(st) (010) OCP/Ap facets.

2.3. *Where does mineralization take place?*

The mineralization process was also monitored *in situ* inside single collagen fibers using spatially resolved confocal Raman spectroscopy (Fig. 5a–c). Here, the gradual shift of the phosphate peak (v_1PO_4), from 957 to 959 cm^{-1}, also confirms the progressive OCP-to-Ap transformation (Fig. 5b and Fig. S5) [23]. To identify the precise location of the growing mineral phase, Raman depth (Z) profiles were collected in collagen fibers after 48 h of maturation (Fig. 5c). The resulting spectra showed that the intensity of the "mineral" peak at 958 cm^{-1} reaches a maximum at the centre of the fiber ($Z = 0$ µm, Fig. 5c), is still observed away from the centre of the fiber ($Z = \pm 50$ µm, Fig. 5c), but becomes negligible in the spectra collected outside the fiber ($Z = \pm 100$ µm, Fig. 5c). SEM observations combined with energy-dispersive X-ray spectroscopy (EDS) analysis on dry mineralized collagen matrices further confirmed the organic/inorganic relationship (Fig. 5d and e). Chemical imaging of the collagen fibers showed that both Ca and P signals of the mineral phase were linked to the N signal of the organic matrix, confirming that the two components were closely related (Fig. 3e). The absence of Ca and P signals outside of the organic matrix further confirmed that mineralization was only taking place within the collagen matrix (Fig. S6).

Thus, our *in situ* observations demonstrate that mineral formation takes place inside the collagen fibers, similarly to natural bone mineralization, where nanocrystals are also formed in the intrafibrillar channels of collagen [44]. Consequently, the nucleation and growth of the mineral phase should perturb the surrounding collagen molecular structure leading to a reduction in the spacing between collagen molecules (*i.e.,* causing compression of the collagen packing) as a function of the mineral content [45–48]. In our *in situ* WAXTS patterns, the broad Bragg peak centred at $Q = 0.42$ $Å^{-1}$ (Fig. 6a) provides information on the intermolecular lateral spacing of the triple-helix collagen molecules [35,46,49,50]. In a non-mineralized sample this peak results in a

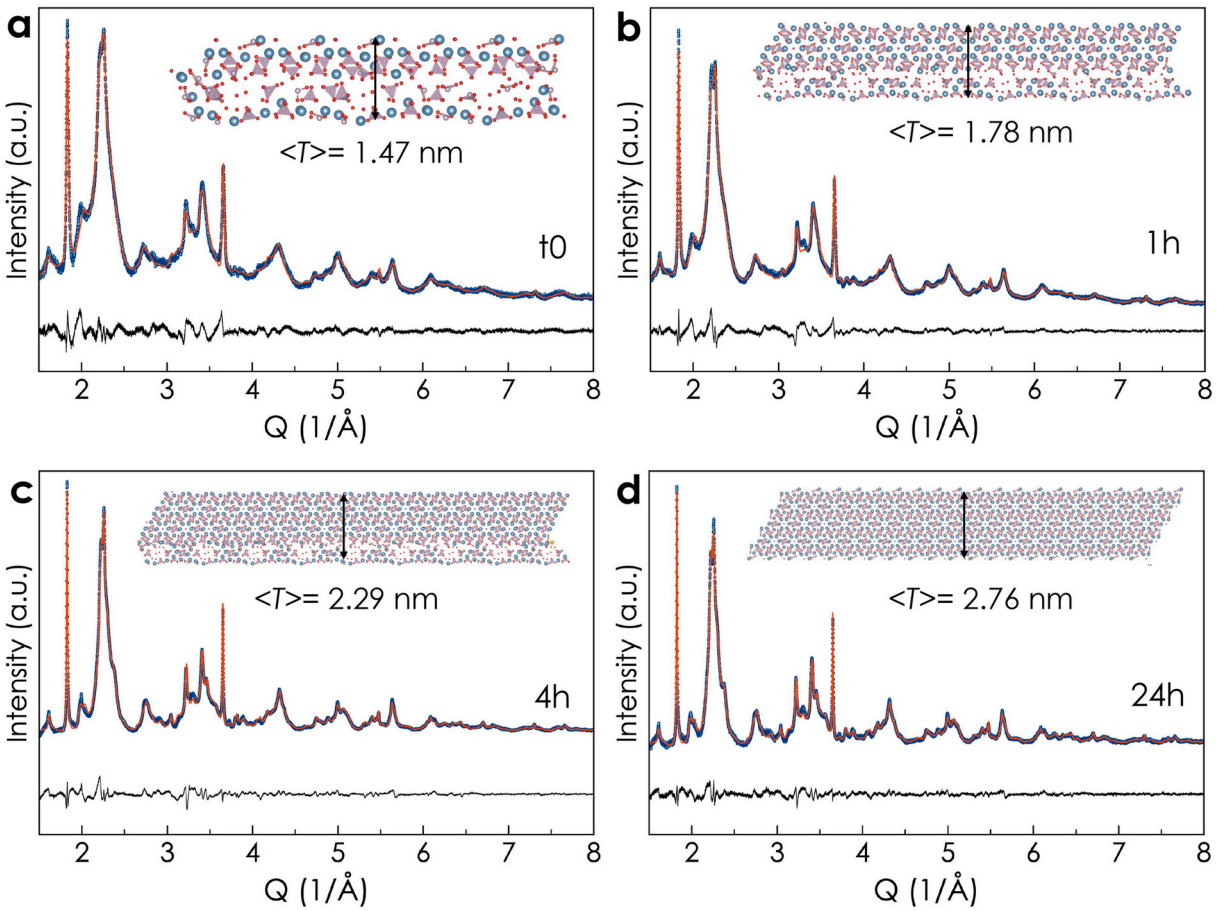

Fig. 4. Best fits for the WAXTS data (blue dots) collected at four different maturation times ($t = 0$, 1, 4 and 24 h) using DSE simulations (red lines) with the OCP/Ap epitaxy according to Xin's model. The average thickness ($<T>$) and structure of the nanoplates are shown as insets. (For interpretation of the references to color in this figure legend, the reader is referred to the Web version of this article.)

d-spacing ($d = 2\pi/Q$) of 14.9 Å[1] (blue trace in Fig. 6a, bottom), which is in good agreement with independent values measured on non-mineralized biological tissues [2,45,50]. During mineralization, this *d*-spacing is indeed reduced, and follows a linear trend with the mineral content (Fig. 6c). At the highest mineral content (see section 4.3), the *d*-spacing is reduced by 0.4 Å (~2.7 %, $d = 14.5$ Å) with respect to the non-mineralized collagen (Fig. 6a). Conversely, in the so-called "dry experiments", described below in Section 4.1, we found that mineral insertion caused a more limited expansion of 0.2 Å (~1.8 %) of the intermolecular contacts, all falling near 11.5 Å (Fig. 6b).

These two (apparently opposite) responses to mineralization can be easily reconciled by the following analysis: *i*) in wet conditions, that is when collagen molecules are soaked into a hydrous environment, a loose packing of the "rod-like" molecules (*ca.* 0.76 molecules nm^{-2}) is present, forced to densify upon mineralization (and water expulsion); *ii*) when, instead, a 60 % denser packing of molecules pre-exists (with *ca.* 1.31 molecules nm^{-2}), as in dry collagen, then the insertion of the mineral automatically swells the molecular arrangement of collagen molecules (insets of Fig. 6a and b). A similar behaviour of the collagen arrangement was observed for dry and wet mineralized biological tissues [46]. In fact, Fig. 6c also shows two linear extrapolations (wet and dry conditions), crossing at *ca.* 11.8 Å (at 46 % mineral content), well in line with the value reported in the literature for such mineralized biological tissues [46] (see supplementary text S2 for further details).

The fact that contraction/expansion (in wet or dry experiments, respectively) of the collagen molecular packing is observed simultaneously with the appearance of the first particles proves that mineralization starts directly in the collagen matrix. These results in combination with Raman and SEM observations, rule out the alternative scenario of particle nucleation in the bulk solution with subsequent infiltration into the fibrils, a frequently proposed view [51,52].

3. Conclusions

We have developed a protocol to study *in situ* the mineralization of dense collagen matrices through the combination of SAXS and WAXTS/DSE analyses. We found that plates of octacalcium phosphate/apatite (OCP/Ap) heterostructures, formed at the early stages of mineralization, gradually transform into the apatite nanoplatelets with morphology and sizes similar to those observed in mature bone. The formation and evolution of this transient epitaxial phase is responsible of the plate-like morphology of bone Ap, breaking the hexagonal crystal symmetry, by a mechanism that was also observed in the presence of important organic players such as citrate and pAsp. Confocal Raman spectroscopy revealed that the transformation of this transient nanocomposite occurs within the collagen fibers. In fact, the evolution of the collagen lateral packing features indicates that the mineralization causes an important distortion of the equatorial arrangement of collagen molecules, following the same trend observed during bone tissue formation. These results shed new light on the early stages of collagen mineralization and, therefore, will

[1] Strictly speaking, following the assumption of a pseudo-hexagonal packing [8], the observed *d*-spacing, corresponding to the 100 reflection, must be transformed into an average intermolecular distance of ca. 13.4 Å by the (often disregarded) $2/\sqrt{3}$ factor, thus providing a more accurate quantitative estimate of the geometrical assembly in the equatorial plane.

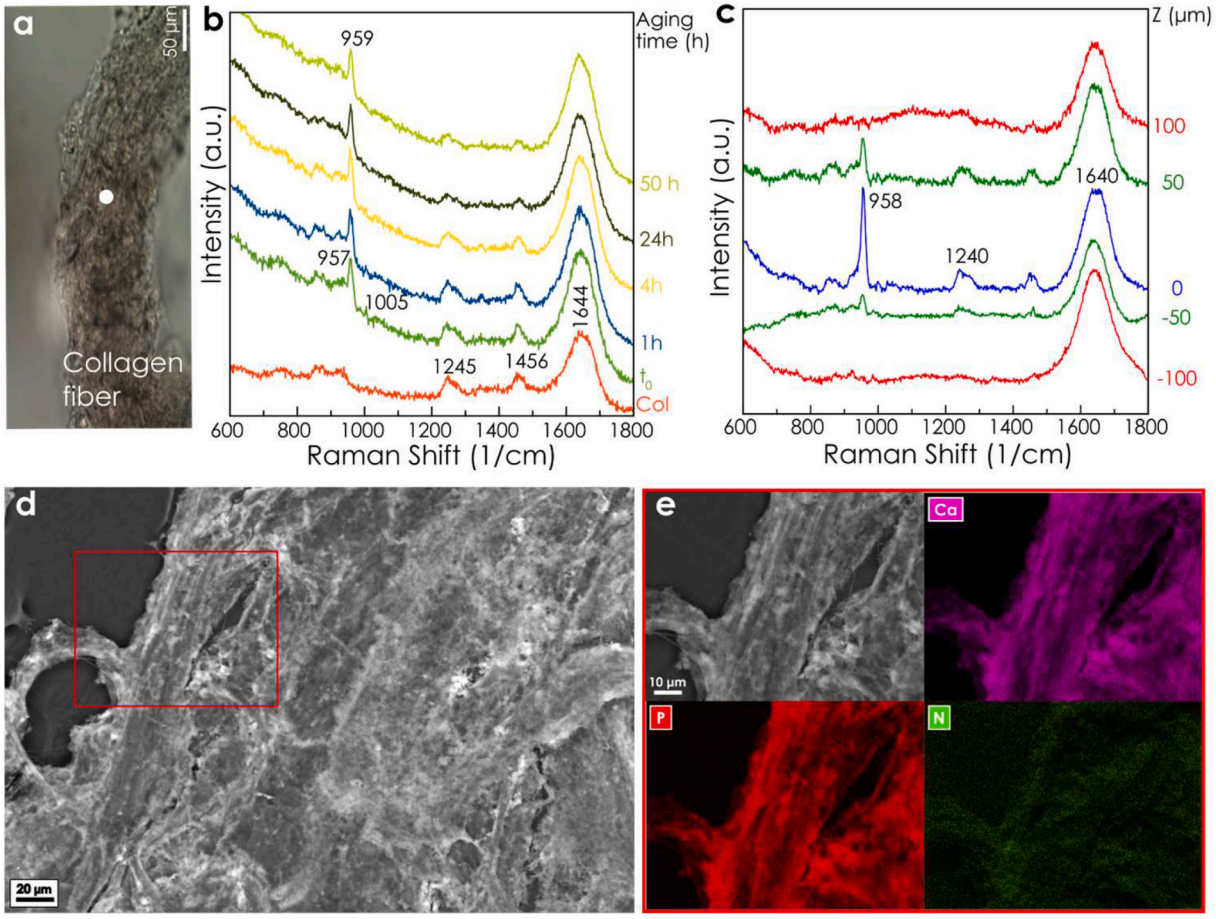

Fig. 5. Identifying the location of the mineral by time-resolved *in situ* Raman spectroscopy and ex-situ SEM. (a) Optical micrograph of the collagen fiber analysed *in situ* with Raman spectroscopy. The Z axis is intended to point out from the picture, towards the reader. (b) Time-dependent Raman spectra collected at increasing maturation times obtained by focusing the beam inside the collagen fiber depicted in (a). The Raman spectrum of a non-mineralized collagen (in PBS) fiber is shown for comparison (red curve). Raman peaks at *ca.* 1245 and 1465 cm^{-1} are the result of the amide III and CH_2 deformation vibrations of type I collagen, respectively [43]. The corresponding symmetric stretching (ν_1PO_4) of the phosphate ions of the mineral phase is shifted from 957 cm^{-1} (ν_1PO_4 of phosphate in an OCP-like structure) to 959 cm^{-1} (ν_1PO_4 of phosphate in an apatite structure) upon maturation. (c) Raman depth profile ($-100 < Z < 100$) showing the mineral distribution within the collagen fiber (aging time: 48 h). (d) SEM micrograph of a dry mineralized collagen matrix. (e) EDS maps, collected from the region marked with the red square in (d), showing the presence of Ca (magenta) and P (red) of the inorganic particles closely related to the N signal of the collagen (green). (For interpretation of the references to color in this figure legend, the reader is referred to the Web version of this article.)

improve our ability to mimic this process in the laboratory to create advanced functional materials in which the organic and inorganic parts are perfectly integrated, resulting in biocompatible nanocomposite materials with high(er) levels of performance. Crystal size and shape of bone mineral are important parameters that affect the strength of hard biological materials such as bone. Thus, the formation of the OCP/Ap heterostructure, which in turn, controls the formation of the extremely thin plates Ap within collagen fibres, may also have important implications for the biomechanical function of bone. However, further experiments are required to determine the specific role of this transient heterostructure in the final mechanical properties of the hybrid materials. In addition, further work can be anticipated in the direction of developing new faster data acquisition methods with instrumental advances and remotely controlled flow-mixing systems to investigate the very early stages of the mineral formation, now hidden in the experimentally limited t_0 value of the SAXS/WAXTS experiments.

4. Methods

4.1. Synthesis of mineralized collagen matrices

Collagen stock solutions: Type I collagen gel was extracted from equine tendon using the standardized manufacturing method of OPOCRIN S.p.A. (Corlo di Formigine, Modena, Italy) as gel [53]. Then, 2 g of this collagen gel were dissolved in 10 mL of acetic acid (0.1 M) by magnetic stirring overnight. The resulting collagen solution was centrifuged at 3000 rpm for 10 min and the supernatant was collected and stored at 4 °C. The pH of this solution was 3.0 and the collagen concentration, measured by UV spectrophotometry, was 1.50 mg mL^{-1}.

Mineralizing solutions: High purity $CaCl_2{\cdot}2H_2O$, Na_2HPO_4, KH_2PO_4, KCl, NaCl and Na_2CO_3 powders were purchased from Sigma-Aldrich. All solutions were prepared with ultrapure deionized water (18 MΩ cm). A phosphate-buffered saline solution (PBS 1x, with the following composition: 10 mM Na_2HPO_4, 1.8 mM KH_2PO_4, 2.7 mM KCl and 137 mM NaCl), pH adjusted to 7.40 with NaOH, was used simultaneously as buffer and phosphate source for all the experiments.

Mineralization Experiments: In comparison to other body fluids, the chemical composition of the extracellular fluids in living bone tissues is enriched in phosphate ions [54]. Hence, to closely mimic the conditions present during *in vivo* bone formation, we used PBS as buffer and phosphate source. Mineralization experiments were carried out at physiological conditions (pH 7.4 and 37 °C) in dense collagen matrices as follows: $CaCl_2$ (final concentration: 2.5 mM) was added to the acidic (pH 3.0) collagen solution. Then, the pH was increased up to 7.40 with

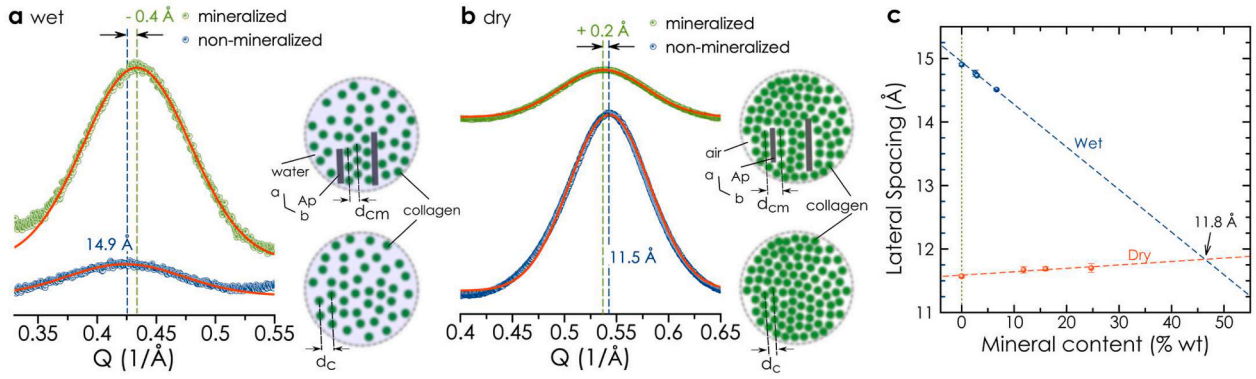

Fig. 6. Evolution, upon mineralization, of the (equatorial) molecular arrangement of collagen within a bundle of parallel and elongated biomolecules (fibril, a section of which is idealized by the circle containing individual molecules – in green). **(a)** Contraction of the lateral packing of collagen molecules upon mineralization as observed by *in situ* (wet) WAXTS experiments. Peak positions were obtained by fitting the experimental data (symbols) with gaussian curves (red lines). The drawings represent the lateral packing of non-mineralized (d_c, bottom) and partially mineralized (d_{cm}, top) collagen fibrils. The replacement of water by apatite nanocrystals results in a contraction ($d_{cm} < d_c$) of the collagen-collagen distances. **(b)** Expansion of the lateral packing observed in dry experiments. In this case, the nanocrystals occupying the intrafibrillar spaces limit the expected collagen shrinkage upon drying ($d_{cm} > d_c$). This situation is also represented in the drawings. **(c)** Plot of the collagen lateral spacing as a function of mineral content (% wt). Blue and red symbols correspond to data extracted from *in situ* (wet) and *ex situ* (dry) WAXTS experiments, respectively. The dotted lines represent the corresponding linear fits. The lateral spacing of the non-mineralized collagen matrices (mineral content = 0 %) in wet (PBS) and dry conditions are 14.9 and 11.5 Å, respectively. (For interpretation of the references to color in this figure legend, the reader is referred to the Web version of this article.)

PBS (final phosphate concentration = 11.8 mM, Ca/P = 0.21), triggering both the simultaneous assembly of collagen into a dense matrix and the onset of mineralization. The formation of dense matrices in the presence of the mineralizing solution has been shown to be a key parameter to induce the formation of intrafibrillar mineralization [10]. The collagen matrix with the corresponding mineralizing solution was rapidly transferred to a 1.0 mm or 2.0 mm glass capillary where the WAXTS and SAXS data (*vide infra*) were sequentially collected. A blank sample containing only collagen in PBS 1x (pH 7.4) was prepared simultaneously (non-mineralized collagen). For the *in situ* Raman experiments the collagen matrix was transferred with the corresponding mineralizing solution to a liquid cell (Fig. S1c). For the characterization of the dry samples, the collagen matrices were left in contact with the mineralizing solutions at 37 °C in a thermostated oven for the desired maturation time. Then, the dense collagen matrix was collected and repeatedly washed with MilliQ water and dried overnight at 37 °C. Using the same protocol and PBS (pH 7.4) as buffer solution and phosphate source, we performed mineralization experiments with higher calcium concentrations, *i.e.*, 20 mM and 40 mM.

Mineralization Experiments in the presence of carbonate and organic additives: Using the lower calcium concentration ($[Ca^{2+}] = 2.5$ mM), the complexity of the mineralization experiments was increased by adding: i) carbonate (final concentration: 5.0 mM) in the PBS buffer (maintaining constant the pH); ii) citrate (final concentration: 5.0 mM) in the $CaCl_2$ solution; iii) poly-aspartic acid (final concentration: 20.0 mM) in the $CaCl_2$ solution.

Rabbit Bone sample: A sample was taken from the femur bone of a young rabbit (approximately 8 months old). The sample was milled and stored at −18 °C before collecting the WAXTS pattern.

4.2. Synchrotron X-ray wide-angle total scattering (WAXTS) measurements

Time-dependent WAXTS experiments were performed on collagen matrices embedded in a 1.0 mm diameter borosilicate glass capillary in contact with the mineralizing solutions (*in situ* mineralization). Patterns were collected at increasing maturation times, from the early stages of mineralization, i.e., 15 min after mixing the collagen and the PBS solutions (t_0), and at selected times up to 40 h of mineralization. Patterns were collected at the X04SA MS-Powder Beamline of the Swiss Light Source (SLS) of the Paul Scherrer Institut (Villigen, Switzerland). 0.8 mm diameter borosilicate glass capillaries were filled with the dry collagen matrices. The beam energy was set at 16 keV and the operational wavelength ($\lambda = 0.77627$ Å) precisely determined by collecting, under the same experimental conditions, a silicon powder standard [NIST 640c, $a_0 = 0.54311946(92)$ nm at 22.5 °C]. Data were collected in a 2-120° 2θ range with the aid of the position sensitive single-photon counting MYTHEN II detector [55]. Data collections were performed at 37 °C using an Oxford Cryojet nitrogen stream. Independent air and empty capillary scattering curves and sample-loaded capillary transmission coefficients were measured and used for data subtraction and absorption corrections. The linear absorption coefficient for the empty capillary was calculated based on the glass composition (Hilgenberg GmbH G50 borosilicate glass).

Determination of the collagen lateral spacing: Following the method reported by Lees et al. [56], the experimental WAXTS peak was fitted by weighted least squares methods using as model the sum of a second-order polynomial (representing a smoothly changing background) and a Gaussian curve, being the peak position used to compute the equatorial spacing of the assembly of "rod-like" collagen molecules ($d = 2\pi/Q$).

4.3. Debye Scattering Equation (DSE)-based data modelling

The Debye scattering equation enables the computation of the total X-ray scattering pattern of randomly oriented non-interacting particles from a set of interatomic distances [57] that can be calculated from atomistic models of nanocrystals. In contrast to the conventional Rietveld method, modelling Bragg intensity only, the DSE does not require any assumption on the structural order and, therefore, provides the ideal tool for modelling the full angular range of WAXTS data collected on nanocrystalline and/or defective materials.

The rearranged equation, following the implementation in the Debussy Suite [58] used for the data analysis is:

$$I(Q) = \sum_{j=1}^{N} f_j(Q)^2 o_j + 2\sum_{j>i=1}^{N} f_j(Q) f_i(Q) T_j(Q) T_i(Q) o_j o_i \frac{\sin(Qd_{ij})}{(Qd_{ij})} \qquad \text{Eq. 1}$$

where $Q = 4\pi \sin\theta/\lambda$ is the scattering vector amplitude, θ is half of the scattering angle 2θ, λ is the radiation wavelength and, for a nanoparticle comprising N atoms, f_j is the atomic form factor of atom j, T_j and o_j describe the isotropic thermal vibration and site-occupancy effects,

respectively ($j = 1, \ldots,N$); d_{ij} is the interatomic distance between i and j atom pairs. According to the DSE standard modeling approach implemented in the Debussy Suite [58], the unit cell content of (nano)crystalline materials, with cell parameters externally adjusted to the experimental data, is used as the building block to generate atomistic models of nanocrystals having a selected shape. Structural defects can be introduced at the atomistic level. Populations of nanocrystals with increasing size are built following mono or bivariate distributions, for isotropic and anisotropic shapes, respectively. Aiming at speeding up calculations, pseudo-multiplicities *vs*. equispaced pair distances are calculated (by applying a Gaussian sampling), instead of the true values and encoded in the generated databases [59]. Structural and microstructural model parameters can be optimized against the experimental data using a simplex minimization algorithm. In the present work, bivariate populations of nanoplates of either OCP/Ap heterostructures or pure Ap were generated and used to calculate WAXTS data with the DSE. Details about the construction of the OCP/Ap epitaxial models used to simulate WAXTS synchrotron data with the DSE are given in the Supporting Information (Text S1), together with the main outcomes of data analysis (Tables S1, S3-S6 and Fig. S4). The mineral content in Fig. 6c and Table S1 was determined by integration of the $<f^2>$-reduced scattering power of the mineral *vs* organic components and represented as % mass mineral in the whole sample.

4.4. Time-resolved in situ small-angle X-ray scattering (SAXS)

Time-resolved *in situ* SAXS measurements reported in this work were performed with a flux-optimized SAXS instrument (Bruker AXS, iNANO, Aarhus University, Denmark) [60,61]. The instrument uses a rotating anode Cu source and homebuilt scatterless slits [62]. A sample-to-detector distance of 0.64 m allowed for a useable Q-range of $0.01 < Q < 0.33$ Å^{-1} where λ in this case is 1.5406 Å. The scattering-range at small-angles was calibrated using a silver behenate powder [63]. SAXS patterns were collected from 2.0 mm borosilicate glass capillaries filled with the collagen matrix and PBS buffer solution (as a blank) and with the mineralizing solution. In the latter experiment, SAXS patterns were repeatedly collected each 15 min to monitor the mineral evolution. SAXS data processing and reduction included primarily masking of undesired pixels, correction of transmission, background subtraction (using as reference the SAXS signal of the capillary filled with PBS) and azimuthal data integration to 1D.

In order to extract the morphological information of the precipitating mineral phases SAXS data of the mineralized samples were further corrected with the corresponding scattering of the collagen matrix (blank). The resulting patterns were fitted by means of least-squares methods [64] with a model suitable to derive the thickness of bone apatite platelets [65]. This model assumes that the mineral particles are elliptical disks with a finite thickness (T), where the thickness is much less than the lateral sizes. A Schulz distribution was used for describing the polydispersity of the thickness, which allowed deriving an analytical expression [35]. Polydispersity was not included for the lateral dimensions. Note that the mathematical expressions are given in the Supplementary Information of [35], except that an elliptical plate shape was used in the present work. Thicknesses and Schulz polydispersity from the time-dependent *in situ* SAXS analysis are shown in Fig. 2b. As per the corresponding lateral dimensions, the thickness-to-disk radius ratio is around 1.5–1.7. These values are in very good agreement with those obtained by WAXTS analysis at comparable aging time (see Table S6).

Furthermore, it turned out to be difficult to fit the low-Q part of the data and to the fit, a dimer structure factor was multiplied on the form factor:

$$S(Q) = 1 + A\,\sin(QR)/(QD) \qquad \text{Eq. 2}$$

where A ($0 \leq A \leq 1$) is the fraction of plates in dimers and D is the average distance between the plates in a dimer. Finally, a Gaussian function was used for describing the Bragg peak of the transient OCP phase.

4.5. Time- and spatially-resolved in situ Raman experiments

In situ Raman measurements were performed with a confocal Raman spectrometer LabRAM-HR (Jobin-Yvon, Horiba) equipped with a Peltier cooled charge-couple device (CCD) (1064 × 256 pixels) detector. The excitation diode laser ($\lambda = 532$ nm) was focused on the sample through a 50 × objective lens (numerical aperture, NA = 0.75) and a pinhole of 50 μm, resulting in a beam cross-sectional diameter of ~2.5 μm. The spectral resolution was 2.0 cm^{-1} (using a grating with 600 grooves mm^{-1}) and each spectrum resulted from averaging 3 acquisitions, with 100 s of accumulation each.

A freshly prepared collagen matrix was immersed in a closed liquid cell (Fig. S1c) and filled with a mineralizing solution. The excitation beam was focused inside a collagen fiber and Raman spectra were sequentially collected each 15 min during the first 4 h, and then each 60 min for another 44 h. Raman depth profiles (Z-maps) were also collected to characterize the typical mineral distribution profile inside a single collagen fiber. Point-by-point Raman spectra were collected at different positions in the direction (Z) normal to the longitudinal axis of the fiber.

4.6. Ex-situ SEM-EDS characterizations of dry collagen

The mineral distribution in dry matrices (maturation: 48 h) was analysed by scanning electron microscopy (SEM) and energy dispersive X-ray spectroscopy (EDS). Freshly washed samples were deposited on amorphous carbon conductive tabs and dried overnight at room temperature. The samples were then carbon-coated and imaged with a beam accelerating voltage of 10 kV using a EVO MA 15 microscope equipped with an 80 mm^2 X-Max^N EDS silicon drift detector (Carl Zeiss Microscopy, LLC, Thornwood, NY). Data were acquired in high-vacuum conditions (10^{-5} mbar).

CRediT authorship contribution statement

Federica Bertolotti: Data curation, Formal analysis, Investigation, Methodology, Writing – review & editing. **Jan Skov Pedersen:** Data curation, Formal analysis, Investigation, Software, Writing – review & editing. **Alexander Van Driessche:** Formal analysis, Investigation, Writing – review & editing. **Norberto Masciocchi:** Conceptualization, Data curation, Formal analysis, Funding acquisition, Investigation, Writing – original draft, Writing – review & editing. **Antonietta Guagliardi:** Conceptualization, Data curation, Funding acquisition, Investigation, Project administration, Supervision, Writing – original draft, Writing – review & editing. **José M. Delgado-López:** Conceptualization, Formal analysis, Funding acquisition, Investigation, Project administration, Writing – original draft, Writing – review & editing.

Declaration of competing interest

The authors declare that they have no known competing financial interests or personal relationships that could have appeared to influence the work reported in this paper.

Data availability

Data will be made available on request.

Acknowledgements

This work has been carried out in the framework of the project BioBone (Andalucía Talent Hub program, co-funded by the Spanish Junta de Andalucía and EU-FP7 within the Marie Skłodowska-Curie

Actions). The authors thank Dr. Michele Iafisco (Institute of Science and Technology for Ceramics, CNR, Italy) for kindly providing the horse tendon collagen used in this work. JMDL and AESVD thank the ESRF and ALBA light-sources for access to beamlines BM2 and BL11-NCD, respectively, where preliminary SAXS/WAXTS experiments were performed. The assistance of the technical staff at the MSX04SA beamline of the SLS (Paul Scherrer Institute) is heartily acknowledged.

Appendix A. Supplementary data

Supplementary data to this article can be found online at https://doi.org/10.1016/j.trac.2024.117904.

Abbreviations

ACP	Amorphous Calcium Phosphate
Ap	Nanocrystalline apatite
DSE	Debye Scattering Equation
EDS	Energy-Dispersive X-ray Spectroscopy
NCP	Non-Collageneous Protein
OCP	Octacalcium Phosphate
PBS	Phosphate-Buffered Saline Solution
SAXS	Small Angle X-ray Scattering
SEM	Scanning Electron Microscopy
TEM	Transmission Electron Microscopy
WAXTS	Wide Angle X-ray Total Scattering

References

[1] M.J. Olszta, X. Cheng, S.S. Jee, R. Kumar, Y.-Y. Kim, M.J. Kaufman, E.P. Douglas, L. B. Gower, Bone structure and formation: a new perspective, Mater. Sci. Eng. R Reports. 58 (2007) 77–116, https://doi.org/10.1016/j.mser.2007.05.001.

[2] P. Fratzl, R. Weinkamer, Nature's hierarchical materials, Prog. Mater. Sci. 52 (2007) 1263–1334. http://www.scopus.com/inward/record.url?eid=2-s2.0-34548501731&partnerID=40&md5=76084760cafd1e1557db4930e92ef2d1.

[3] W. Landis, R. Jacquet, Association of calcium and phosphate ions with collagen in the mineralization of vertebrate tissues, Calcif. Tissue Int. 93 (2013) 329–337, https://doi.org/10.1007/s00223-013-9725-7.

[4] S. Weiner, H.D. Wagner, The material bone: structure-mechanical function relations, Annu. Rev. Mater. Sci. 28 (1998) 271–298. 10.1146/annurev.matsci.28.1.271.

[5] J.Y. Rho, L. Kuhn-Spearing, P. Zioupos, Mechanical properties and the hierarchical structure of bone, Med. Eng. Phys. 20 (1998) 92–102. http://www.scopus.com/inward/record.url?eid=2-s2.0-0032029664&partnerID=40&md5=639e2c5267d41c8522e9b8e1737c7585.

[6] W.J. Landis, K.J. Hodgens, M.J. Song, J. Arena, S. Kiyonaga, M. Marko, C. Owen, B. F. McEwen, Mineralization of collagen may occur on fibril surfaces: evidence from conventional and high-voltage electron microscopy and three-dimensional imaging, J. Struct. Biol. 117 (1996) 24–35, https://doi.org/10.1006/jsbi.1996.0066.

[7] B.M. Oosterlaken, M.P. Vena, G. de With, In vitro mineralization of collagen, Adv. Mater. 33 (2021) 2004418, https://doi.org/10.1002/adma.202004418.

[8] C. Combes, C. Rey, Amorphous calcium phosphates: synthesis, properties and uses in biomaterials, Acta Biomater. 6 (2010) 3362–3378, https://doi.org/10.1016/j.actbio.2010.02.017.

[9] A. George, A. Veis, Phosphorylated proteins and control over apatite nucleation, crystal growth, and inhibition, Chem. Rev. 108 (2008) 4670–4693, https://doi.org/10.1021/cr0782729.

[10] Y. Wang, T. Azaïs, M. Robin, A. Vallée, C. Catania, P. Legriel, G. Pehau-Arnaudet, F. Babonneau, M.-M. Giraud-Guille, N. Nassif, The predominant role of collagen in the nucleation, growth, structure and orientation of bone apatite, Nat. Mater. 11 (2012) 724–733. http://www.nature.com/nmat/journal/v11/n8/abs/nmat3362.html#supplementary-information.

[11] H.A. Lowenstam, S. Weiner, On Biomineralization, University Press, Oxford, 1989.

[12] S.J. Eppell, W. Tong, J.L. Katz, L. Kuhn, M.J. Glimcher, Shape and size of isolated bone mineralites measured using atomic force microscopy, J. Orthop. Res. 19 (2001) 1027–1034, https://doi.org/10.1016/S0736-0266(01)00034-1.

[13] P. Fratzl, H.S. Gupta, E.P. Paschalis, P. Roschger, Structure and mechanical quality of the collagen-mineral nano-composite in bone, J. Mater. Chem. 14 (2004) 2115–2123, https://doi.org/10.1039/b402005g.

[14] M.I. Kay, R.A. Young, A.S. Posner, Crystal structure of hydroxyapatite, Nature 204 (1964) 1050–1052, https://doi.org/10.1038/2041050a0.

[15] J.C. Elliott, P.E. Mackie, R.A. Young, Monoclinic hydroxyapatite, Science 180 (1973) 1055–1057, https://doi.org/10.1126/science.180.4090.1055.

[16] T. Leventouri, Synthetic and biological hydroxyapatites: crystal structure questions, Biomaterials 27 (2006) 3339–3342, https://doi.org/10.1016/j.biomaterials.2006.02.021.

[17] Y.Y. Hu, A. Rawal, K. Schmidt-Rohr, Strongly bound citrate stabilizes the apatite nanocrystals in bone, Proc. Natl. Acad. Sci. U.S.A. 107 (2010) 22425–22429, https://doi.org/10.1073/pnas.1009219107.

[18] E. Davies, K.H. Müller, W.C. Wong, C.J. Pickard, D.G. Reid, J.N. Skepper, M. J. Duer, Citrate bridges between mineral platelets in bone, Proc. Natl. Acad. Sci. USA (2014), https://doi.org/10.1073/pnas.1315080111.

[19] J.M. Delgado-López, R. Frison, A. Cervellino, J. Gómez-Morales, A. Guagliardi, N. Masciocchi, Crystal size, morphology, and growth mechanism in bio-inspired apatite nanocrystals, Adv. Funct. Mater. 24 (2014) 1090–1099.

[20] A.C. Deymier, A.K. Nair, B. Depalle, Z. Qin, K. Arcot, C. Drouet, C.H. Yoder, M. J. Buehler, S. Thomopoulos, G.M. Genin, J.D. Pasteris, Protein-free formation of bone-like apatite: new insights into the key role of carbonation, Biomaterials 127 (2017) 75–88, https://doi.org/10.1016/j.biomaterials.2017.02.029.

[21] J. Mahamid, A. Sharir, L. Addadi, S. Weiner, Amorphous calcium phosphate is a major component of the forming fin bones of zebrafish: indications for an amorphous precursor phase, Proc. Natl. Acad. Sci. USA 105 (2008) 12748–12753, https://doi.org/10.1073/pnas.0803354105.

[22] J. Mahamid, B. Aichmayer, E. Shimoni, R. Ziblat, C. Li, S. Siegel, O. Paris, P. Fratzl, S. Weiner, L. Addadi, Mapping amorphous calcium phosphate transformation into crystalline mineral from the cell to the bone in zebrafish fin rays, Proc. Natl. Acad. Sci. USA 107 (2010) 6316–6321, https://doi.org/10.1073/pnas.0914218107.

[23] N.J. Crane, V. Popescu, M.D. Morris, P. Steenhuis, M.A. Ignelzi Jr., Raman spectroscopic evidence for octacalcium phosphate and other transient mineral species deposited during intramembranous mineralization, Bone 39 (2006) 434–442, https://doi.org/10.1016/j.bone.2006.02.059.

[24] W.E. Brown, J.P. Smith, J.R. Lehr, A.W. Fraizer, Octacalcium phosphate and hydroxyapatite: crystallographic and chemical relations between octacalcium phosphate and hydroxyapatite, Nature 196 (1962) 1050–1055, https://doi.org/10.1038/1961050a0.

[25] W.E. Brown, N. Eidelman, B. Tomazic, Octacalcium phosphate as a precursor in biomineral formation, Adv. Dent. Res. 1 (1987) 306–313, https://doi.org/10.1177/08959374870010022201.

[26] J. Tao, K.C. Battle, H. Pan, E.A. Salter, Y.-C. Chien, A. Wierzbicki, J.J. De Yoreo, Energetic basis for the molecular-scale organization of bone, Proc. Natl. Acad. Sci. USA 112 (2015) 326–331, https://doi.org/10.1073/pnas.1404481112.

[27] J.M. Delgado-López, R. Frison, A. Cervellino, J. Gómez-Morales, A. Guagliardi, N. Masciocchi, Crystal size, morphology, and growth mechanism in bio-inspired apatite nanocrystals, Adv. Funct. Mater. 24 (2014) 1090–1099, https://doi.org/10.1002/adfm.201302075.

[28] G. Dal Sasso, M.C. Dalconi, G. Ferrari, J.S. Pedersen, S. Tamburini, F. Bertolotti, A. Guagliardi, M. Bruno, L. Valentini, G. Artioli, An atomistic model describing the structure and morphology of Cu-doped C-S-H hardening accelerator nanoparticles, Nanomaterials 12 (2022), https://doi.org/10.3390/nano12030342.

[29] D. Moscheni, F. Bertolotti, L. Piveteau, L. Protesescu, D.N. Dirin, M. V Kovalenko, A. Cervellino, J.S. Pedersen, N. Masciocchi, A. Guagliardi, Size-dependent fault-driven relaxation and faceting in zincblende CdSe colloidal quantum dots, ACS Nano 12 (2018) 12558–12570, https://doi.org/10.1021/acsnano.8b07092.

[30] F. Bertolotti, D.N. Dirin, M. Ibáñez, F. Krumeich, A. Cervellino, R. Frison, O. Voznyy, E.H. Sargent, M. V Kovalenko, A. Guagliardi, N. Masciocchi, Crystal symmetry breaking and vacancies in colloidal lead chalcogenide quantum dots, Nat. Mater. 15 (2016) 987–994, https://doi.org/10.1038/nmat4661.

[31] F. Bertolotti, L. Protesescu, M. V Kovalenko, S. Yakunin, A. Cervellino, S.J. L. Billinge, M.W. Terban, J.S. Pedersen, N. Masciocchi, A. Guagliardi, Coherent nanotwins and dynamic disorder in cesium lead halide perovskite nanocrystals, ACS Nano 11 (2017) 3819–3831, https://doi.org/10.1021/acsnano.7b00017.

[32] F. Bertolotti, A. Vivani, F. Ferri, P. Anzini, A. Cervellino, M.I. Bodnarchuk, G. Nedelcu, C. Bernasconi, M. V Kovalenko, N. Masciocchi, A. Guagliardi, Size segregation and atomic structural coherence in spontaneous assemblies of colloidal cesium lead halide nanocrystals, Chem. Mater. 34 (2022) 594–608, https://doi.org/10.1021/acs.chemmater.1c03162.

[33] F.J. Carmona, G. Dal Sasso, F. Bertolotti, G.B. Ramírez-Rodríguez, J.M. Delgado-López, J.S. Pedersen, N. Masciocchi, A. Guagliardi, The role of nanoparticle structure and morphology in the dissolution kinetics and nutrient release of nitrate-doped calcium phosphate nanofertilizers, Sci. Rep. 10 (2020) 12396, https://doi.org/10.1038/s41598-020-69279-2.

[34] F. Bertolotti, F.J. Carmona, G. Dal Sasso, G.B. Ramírez-Rodríguez, J.M. Delgado-López, J.S. Pedersen, F. Ferri, N. Masciocchi, A. Guagliardi, On the amorphous layer in bone mineral and biomimetic apatite: a combined small- and wide-angle X-ray scattering analysis, Acta Biomater. 120 (2021) 167–180, https://doi.org/10.1016/j.actbio.2020.04.026.

[35] J.M. Delgado-López, F. Bertolotti, J. Lyngsø, J.S. Pedersen, A. Cervellino, N. Masciocchi, A. Guagliardi, The synergic role of collagen and citrate in stabilizing amorphous calcium phosphate precursors with platy morphology, Acta Biomater. 49 (2017), https://doi.org/10.1016/j.actbio.2016.11.041.

[36] K. Chatzipanagis, M. Iafisco, T. Roncal-Herrero, M. Bilton, A. Tampieri, R. Kröger, J.M. Delgado-López, Crystallization of citrate-stabilized amorphous calcium phosphate to nanocrystalline apatite: a surface-mediated transformation, CrystEngComm 18 (2016), https://doi.org/10.1039/c6ce00521g.

[37] D. Kim, B. Lee, S. Thomopoulos, Y.-S. Jun, The role of confined collagen geometry in decreasing nucleation energy barriers to intrafibrillar mineralization, Nat. Commun. 9 (2018) 962, https://doi.org/10.1038/s41467-018-03041-1.

[38] R. Xin, Y. Leng, N. Wang, In situ TEM examinations of octacalcium phosphate to hydroxyapatite transformation, J. Cryst. Growth 289 (2006) 339–344, https://doi.org/10.1016/j.jcrysgro.2005.11.010.

[39] J. Gómez-Morales, M. Iafisco, J.M. Delgado-López, S. Sarda, C. Drouet, Progress on the preparation of nanocrystalline apatites and surface characterization:

fundamental and applied overviews, Prog. Cryst. Growth Charact. Accepted (2012).
[40] M. Mathew, W.E. Brown, L.W. Schroeder, B. Dickens, Crystal structure of octacalcium bis(hydrogenphosphate) tetrakis(phosphate)pentahydrate, Ca8(HP04) 2(PO4)4·5H2O, J. Crystallogr. Spectrosc. Res. 18 (1988) 235–250, https://doi.org/10.1007/BF01194315.
[41] W.E. Brown, Octacalcium phosphate and hydroxyapatite, Nature 196 (1962) 1048–1050, https://doi.org/10.1038/1961048b0.
[42] M.E. Fernández, C. Zorrilla-Cangas, R. García-García, J.A. Ascencio, J. Reyes-Gasga, New model for the hydroxyapatite-octacalcium phosphate interface, Acta Crystallogr. B 59 (2003) 175–181, https://doi.org/10.1107/S0108768103002167.
[43] G.S. Mandair, M.D. Morris, Contributions of Raman spectroscopy to the understanding of bone strength, BoneKEy Rep. 4 (2015), https://doi.org/10.1038/bonekey.2014.115.
[44] C. Burger, H. Zhou, H. Wang, I. Sics, B.S. Hsiao, B. Chu, L. Graham, M.J. Glimcher, Lateral packing of mineral crystals in bone collagen fibrils, Biophys. J. 95 (2008) 1985–1992, https://doi.org/10.1529/biophysj.107.128355.
[45] P. Fratzl, N. Fratzl-Zelman, K. Klaushofer, Collagen packing and mineralization. An x-ray scattering investigation of Turkey leg tendon, Biophys. J. 64 (1993) 260–266, https://doi.org/10.1016/S0006-3495(93)81362-6.
[46] S. Lees, Mineralization of type I collagen, Biophys. J. 85 (2003) 204–207. http://www.ncbi.nlm.nih.gov/pmc/articles/PMC1303077/.
[47] S. Lees, Interpreting the equatorial diffraction pattern of collagenous tissues in the light of molecular motion, Biophys. J. 75 (1998) 1058–1061. http://www.ncbi.nlm.nih.gov/pmc/articles/PMC1299780/.
[48] S. Lees, A mixed packing model for bone collagen, Calcif. Tissue Int. 33 (1981) 591–602, https://doi.org/10.1007/BF02409497.
[49] L.C. Bonar, S. Lees, H.A. Mook, Neutron diffraction studies of collagen in fully mineralized bone, J. Mol. Biol. 181 (1985) 265–270, https://doi.org/10.1016/0022-2836(85)90090-7.
[50] E.D. Eanes, D.R. Lundy, G.N. Martin, X-ray diffraction study of the mineralization of Turkey leg tendon, Calcif. Tissue Res. 6 (1970) 239–248. http://www.ncbi.nlm.nih.gov/pubmed/5500677.
[51] F. Nudelman, K. Pieterse, A. George, P.H.H. Bomans, H. Friedrich, L.J. Brylka, P.A. J. Hilbers, G. de With, N. Sommerdijk, The role of collagen in bone apatite formation in the presence of hydroxyapatite nucleation inhibitors, Nat. Mater. 9 (2010) 1004–1009, https://doi.org/10.1038/nmat2875.
[52] L.B. Gower, Biomimetic model systems for investigating the amorphous precursor pathway and its role in biomineralization, Chem. Rev. 108 (2008) 4551–4627, https://doi.org/10.1021/cr800443h.
[53] A. Tampieri, G. Celotti, E. Landi, M. Sandri, N. Roveri, G. Falini, Biologically inspired synthesis of bone-like composite: self-assembled collagen fibers/hydroxyapatite nanocrystals, J. Biomed. Mater. Res., Part A 67A (2003) 618–625, https://doi.org/10.1002/jbm.a.10039.
[54] A.S. Deshpande, E. Beniash, Bioinspired synthesis of mineralized collagen fibrils, Cryst. Growth Des. 8 (2008) 3084–3090, https://doi.org/10.1021/cg800252f.
[55] A. Bergamaschi, A. Cervellino, R. Dinapoli, F. Gozzo, B. Henrich, I. Johnson, P. Kraft, A. Mozzanica, B. Schmitt, X. Shi, The MYTHEN detector for X-ray powder diffraction experiments at the Swiss Light Source, J. Synchrotron Radiat. 17 (2010) 653–668, https://doi.org/10.1107/S0909049510026051.
[56] S. Lees, L.C. Bonar, H.A. Mook, A study of dense mineralized tissue by neutron diffraction, Int. J. Biol. Macromol. 6 (1984) 321–326, https://doi.org/10.1016/0141-8130(84)90017-5.
[57] P. Debye, Zerstreuung von Röntgenstrahlen, Ann. Phys. 351 (1915) 809–823, https://doi.org/10.1002/andp.19153510606.
[58] A. Cervellino, R. Frison, F. Bertolotti, A. Guagliardi, Debussy 2.0: the new release of a Debye user system for nanocrystalline and/or disordered materials, J. Appl. Crystallogr. 48 (2015) 2026–2032, https://doi.org/10.1107/S1600576715020488.
[59] A. Cervellino, C. Giannini, A. Guagliardi, On the efficient evaluation of Fourier patterns for nanoparticles and clusters, J. Comput. Chem. 27 (2006) 995–1008, https://doi.org/10.1002/jcc.20407.
[60] A. Schwamberger, B. De Roo, D. Jacob, L. Dillemans, L. Bruegemann, J.W. Seo, J. P. Locquet, Combining SAXS and DLS for simultaneous measurements and time-resolved monitoring of nanoparticle synthesis, Nucl. Instrum. Methods Phys. Res. Sect. B Beam Interact. Mater. Atoms 343 (2015) 116–122, https://doi.org/10.1016/j.nimb.2014.11.049.
[61] J. Lyngsø, J.S. Pedersen, A high-flux automated laboratory small-angle X-ray scattering instrument optimized for solution scattering, J. Appl. Crystallogr. 54 (2021) 295–305, https://doi.org/10.1107/S1600576720016209.
[62] Y. Li, R. Beck, T. Huang, M.C. Choi, M. Divinagracia, Scatterless hybrid metal-single-crystal slit for small-angle X-ray scattering and high-resolution X-ray diffraction, J. Appl. Crystallogr. 41 (2008) 1134–1139, https://doi.org/10.1107/S0021889808031129.
[63] T.C. Huang, H. Toraya, T.N. Blanton, Y. Wu, X-ray powder diffraction analysis of silver behenate, a possible low-angle diffraction standard, J. Appl. Crystallogr. 26 (1993) 180–184, https://doi.org/10.1107/S0021889892009762.
[64] J.S. Pedersen, Analysis of small-angle scattering data from colloids and polymer solutions: modeling and least-squares fitting, Adv. Colloid Interface Sci. 70 (1997) 171–210, https://doi.org/10.1016/S0001-8686(97)00312-6.
[65] M.H. Bünger, H. Oxlund, T.K. Hansen, S. Sørensen, B.M. Bibby, J.S. Thomsen, B. L. Langdahl, F. Besenbacher, J.S. Pedersen, H. Birkedal, Strontium and bone nanostructure in normal and ovariectomized rats investigated by scanning small-angle X-ray scattering, Calcif. Tissue Int. 86 (2010) 294–306, https://doi.org/10.1007/s00223-010-9341-8.